

See discussions, stats, and author profiles for this publication at: <https://www.researchgate.net/publication/231647249>

# Periodic DFT and HR-STEM Studies of Surface Structure and Morphology of Cobalt Spinel Nanocrystals. Retrieving 3D Shapes from 2D Images

ARTICLE *in* THE JOURNAL OF PHYSICAL CHEMISTRY C · MARCH 2011

Impact Factor: 4.77 · DOI: 10.1021/jp200581s

---

CITATIONS

21

READS

134

---

## 8 AUTHORS, INCLUDING:



[Witold Piskorz](#)

Jagiellonian University

84 PUBLICATIONS 389 CITATIONS

[SEE PROFILE](#)



[Paweł Stelmachowski](#)

Jagiellonian University

61 PUBLICATIONS 339 CITATIONS

[SEE PROFILE](#)



[Andrzej Kotarba](#)

Jagiellonian University

130 PUBLICATIONS 1,061 CITATIONS

[SEE PROFILE](#)



[Tomasz Płociński](#)

Warsaw University of Technology

51 PUBLICATIONS 313 CITATIONS

[SEE PROFILE](#)

# Periodic DFT and HR-STEM Studies of Surface Structure and Morphology of Cobalt Spinel Nanocrystals. Retrieving 3D Shapes from 2D Images

Filip Zasada,<sup>†</sup> Witold Piskorz,<sup>†</sup> Paweł Stelmachowski,<sup>†</sup> Andrzej Kotarba,<sup>†</sup> Jean-François Paul,<sup>‡</sup> Tomasz Płociński,<sup>§</sup> Krzysztof J. Kurzydłowski,<sup>§</sup> and Zbigniew Sojka<sup>†,\*</sup>

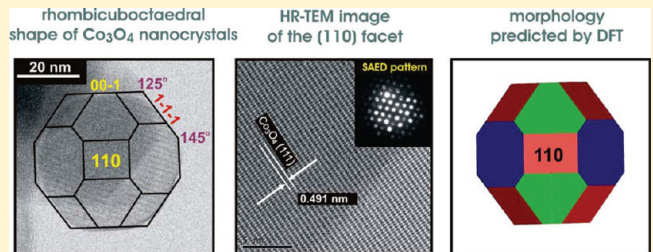
<sup>†</sup>Department of Chemistry, Jagiellonian University, Ingardena 3, 30-060 Krakow, Poland

<sup>‡</sup>Laboratoire de Modélisation et Spectroscopie UCCS, l'Université des Sciences et Technologies de Lille, Villeneuve d'Ascq, France

<sup>§</sup>Faculty of Materials Science and Engineering, Warsaw University of Technology, Wołoska 141, 02-507 Warsaw, Poland

 Supporting Information

**ABSTRACT:** In this study, we investigated the morphology of  $\text{Co}_3\text{O}_4$  nanocrystals using periodic PW91 and PW91+U density functional calculations and Wulff construction. Theoretical investigations were combined with high resolution scanning transmission electron microscopy, which revealed that the examined spinel samples, obtained by pH-controlled precipitation, exhibit well-developed faceted crystallites. The results of slab calculations enabled to characterize the surface structure and reconstruction of the low index (100), (110), and (111) planes that were observed in HR-STEM pictures. The surface energies of the relaxed facets increased in the following order  $1.39 \text{ J m}^{-2}$  (100)  $< 1.48 \text{ J m}^{-2}$  (111)  $< 1.65 \text{ J m}^{-2}$  (110). These ab initio calculated values were used to predict a rhombicuboctaedral equilibrium habit of the cobalt spinel crystallites, by means of the Wulff plot. The obtained results were in remarkable agreement with the experimental shapes retrieved by matching 3D Wulff polyhedra to 2D STEM images observed along three different [100], [110], and [111] directions. Thus, the joined theoretical and experimental approach applied successfully herein, allowed not only for univocal shape determination and surface structure reconstruction of the faceted  $\text{Co}_3\text{O}_4$  nanocrystals, but also provided the in-depth understanding of the observed features at the atomic level.



## INTRODUCTION

Many important properties of nanostructured oxides depend on their size, dimensionality and shape.<sup>1–4</sup> Obvious examples include optical, electronic and magnetic properties, interfacial phenomena and chemical reactivity.<sup>5–7</sup> Owing to the clear-cut structure and substantial surface area, oxide nanocrystals provide excellent model systems for joined experimental and theoretical investigations into surface related properties at nanometric scale, in more realistic pressure and temperature conditions, than in the case of conventional high vacuum single crystal studies.<sup>8–10</sup> Faceted polyhedral crystals expose well-defined crystallographic planes, depending on the synthesis method, allowing for sensible investigations into structure–reactivity relationships at practical conditions.<sup>11–13</sup> This assists in designing of new catalytic materials of enhanced activity and selectivity by preferential development of more active planes or by enhancement of the density of active sites.<sup>11</sup>

From the thermodynamic point of view, the equilibrium shape of a nanocrystal is determined by the free energies of various facets  $\gamma_{hkl}(n)$ , and can be revealed by classic Wulff construction that minimizes the total surface free energy at a fixed volume.<sup>14</sup> The Wulff theorem provides a simple relation between the  $\gamma_{hkl}(n)$

energy of the  $(hkl)$  plane and its distance  $r_{hkl}$  in the normal direction  $n$  from the center of the crystallite. Later on, the thermodynamic stability of faceted and rounded shapes was revisited by Herring.<sup>15</sup> In the case when the morphology of a nanocrystal is known from microscopic observations,  $\gamma(n)$  can be assessed by iterative way until the resulting shape matches the observed one, by using Wulff construction in the inverse fashion.<sup>16</sup> In addition to the thermodynamic driving forces, kinetics also plays an important role in determination of the morphology in the real growth conditions. In such a case, the approach advanced by Chernov can be applied to predict the steady-state shapes of nanocrystals.<sup>17</sup>

In recent years sophisticated tools, such as synchrotron X-ray diffraction, scanning probe microscopy, Cs-corrected high resolution transmission electron microscopy,<sup>18</sup> or electron tomography<sup>19,20</sup> have been applied for nanocrystals characterization and to retrieve correct and comprehensive structural and morphological information. Yet, several challenges still remain, especially with regard to 3-D

Received: January 19, 2011

Revised: March 1, 2011

Published: March 22, 2011

**Table 1.** Supercell Parameters of Different  $\text{Co}_3\text{O}_4$  Planes

		supercell	supercell size	number of $\text{Co}_3\text{O}_4$ units/stoichiometry
(100)	regular	$\alpha = \beta = \gamma = 90^\circ$	$a = b = 8.051 \text{ \AA}$ $c = 20.061 \text{ \AA}$	10/ $\text{Co}_{30}\text{O}_{40}$
(110)	regular	$\alpha = \beta = \gamma = 90^\circ$	$a = 8.051 \text{ \AA}, b = 11.388 \text{ \AA}$ $c = 18.544 \text{ \AA}$	14/ $\text{Co}_{42}\text{O}_{56}$
(111)	hexagonal	$\alpha = \beta = 90^\circ, \gamma = 120^\circ$	$a = b = 11.388 \text{ \AA}$ $c = 20.460 \text{ \AA}$	16/ $\text{Co}_{48}\text{O}_{64}$

reconstruction of the nanocrystals shape. To reach a satisfactory tomographic reconstruction, for instance, some essential aspects of the acquisition procedure such as application of special high tilt holders preventing shadowing of the viewable grid area, use of small tilt increments, precise alignment of the component images should be carefully addressed.<sup>19,20</sup>

Owing to recent progress in computational chemistry, fairly accurate first principles calculations of nanoparticles surface structure and theoretical predictions of the resultant nanomorphology are made possible.<sup>5,10,21</sup> By invoking a simple approach of the Wulff construction along with the *ab initio* thermodynamics one can account also for more realistic environment conditions.<sup>21</sup> For number of nanomaterials, such approach has proved its excellent predictive and explanatory capabilities. It has been used, for instance, to examine the equilibrium geometry of titanium dioxide<sup>22,23</sup> and alumina polymorphs,<sup>24</sup> maghemite,<sup>25,26</sup> magnesium oxide in dry and wet conditions,<sup>27</sup> as well as lead oxide in arbitrary oxygen pressure.<sup>28</sup> Convergence of theory with high resolution electron microscopy becomes especially productive for detailed understanding the habit of nanocrystals, their surface structure and for shape modeling as well. Examples are provided by thorough investigations of MgO by Jupille et al.<sup>27</sup> or by Stroppa et al. work on antimony-doped tin dioxide.<sup>29</sup>

The cobalt spinel belongs to one of the most attractive oxides with remarkable record of widespread applications.<sup>11,30,31,32</sup> In particular  $\text{Co}_3\text{O}_4$  frequently used as a catalyst,<sup>33–35</sup> has recently received a great deal of theoretical and practical attention because of its outstanding activity in low temperature decomposition of  $\text{N}_2\text{O}$ .<sup>36–38</sup> Noting the particular structure with disparate concentration of the active sites it is not surprising that distinct surface planes of  $\text{Co}_3\text{O}_4$  exhibit different activities. Shape-dependent oxygen storage capacity of ceria nanocrystals<sup>39</sup> and carbon monoxide oxidation over nanostructured cobalt spinel,<sup>11</sup> may serve here as paramount examples.

In the present work we investigated the surface properties and the shape of  $\text{Co}_3\text{O}_4$  spinel by *ab initio* periodic calculations based on DFT theory. The surface geometry relaxation and stability of the exposed low index (100), (110), and (111) planes were examined in detail. We use combination of the information obtained from images taken by high resolution Cs-corrected STEM and the calculated DFT surface energies for three-dimensional Wulff reconstruction of the shape of spinel nanocrystals. Despite widespread use of the cobalt spinel there are only few theoretical papers devoted to explicit DFT calculations of  $\text{Co}_3\text{O}_4$ ,<sup>34,40</sup> but no one has been dealing with surface structure and morphology elucidation as yet.

## EXPERIMENTAL SECTION

**Calculation Details.** For all calculations DFT level of theory was chosen with use of the Vienna *ab initio* simulations package

(VASP)<sup>41</sup> based on Mermin's finite temperature DFT.<sup>42</sup> Projector augmented plane wave (PAW)<sup>43,44</sup> method for describing electron-ion interactions together with generalized gradient GGA-PW91 exchange-functional as parametrized by Perdew et al.<sup>45</sup> were employed. In addition to DFT scheme, in accounting for electron correlation effects the DFT+U method developed by Anisimov was used. While the values of  $U$  from 2 to 5 eV, all produced qualitatively similar results in terms of the converged electronic structure, eventually the value of the Hubbard parameter equal to  $U = 3.5$  eV was used, in accordance with earlier papers.<sup>46</sup> The DFT+U calculations were performed only to describe bulk properties, since they had little influence on the calculated surface properties (*vide infra*).

A number of tests were initially performed to verify the accuracy of the method (cutoff energy from 350 to 500 eV and  $k$ -point set from  $1 \times 1 \times 1$  to  $5 \times 5 \times 5$ ). As a result all slab calculations were performed using standard Monkhorst-Pack<sup>47</sup> grid ( $2 \times 2 \times 1$  sampling mesh) with cutoff energy of 400 eV and a Methfessel–Paxton<sup>48</sup> smearing with  $\sigma$  parameter set to 0.1 eV. For solving the Kohn–Sham SCF convergence, a constraint was set to be an energy change of  $10^{-5}$  eV between two successive iterations. The geometry optimization of  $\text{Co}_3\text{O}_4$  indicated that for bulk calculations a good agreement between predicted and experimental structure<sup>49</sup> was obtained. Surface geometries were constructed by cleaving the solid in the normal (100), (110), and (111) directions, thus obtaining large supercells containing ca. 10 atomic layers. Vacuum space of 10 Å was located above modeled surfaces in the  $z$  direction to separate oxides layers from the interactions (Table 1).

The stoichiometry of the bulk  $\text{Co}_3\text{O}_4$  was preserved in the constructed slab model, together with the tetrahedral to octahedral cobalt ratio of 1:2. Furthermore, the same structure of the top and the bottom slab terminations was ascertained. Relaxation of the atomic positions in the four top layers was assumed to render forces acting upon the ions below  $1 \times 10^{-2} \text{ eV} \cdot \text{\AA}^{-1}$ .

The Wulffman program<sup>16,50</sup> in tandem with Geomview interactive 3D visualization software<sup>51</sup> were used to predict theoretical equilibrium habit of the nanocrystals (minimum surface energy convex polyhedra), following the rule

$$\gamma_{hkl}(n)/r_{hkl} = \text{constant}, \quad \forall hkl \quad (1)$$

where  $\gamma_{hkl}$  is the surface energy of the exposed  $(hkl)$  plane and  $r_{hkl}$  is the distance from the center of the nanocrystal to the surface of the  $hkl$  plane.

**Materials and Characterization.** The  $\text{Co}_3\text{O}_4$  spinel samples were prepared by pH-controlled precipitation method as described elsewhere in more detail.<sup>36,37</sup> The samples were calcined at 400 °C in air for 2 h prior characterization measurements. The phase verification of the synthesized material was performed by

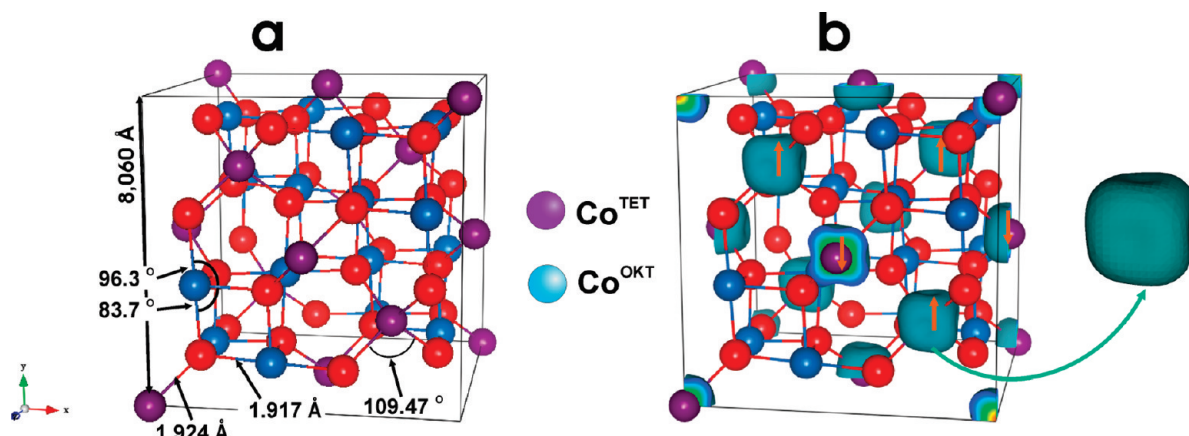


**Figure 1.** (a) Illustration of the cubic  $\text{Co}_3\text{O}_4$  spinel structure. The  $\text{Co}^{2+}$  ions, colored blue, occupy tetrahedral sites and the  $\text{Co}^{3+}$  ions, colored purple, occupy octahedral sites within a fcc oxygen sublattice, colored red. (b) Spin density repartition revealing two networks of paramagnetic tetrahedral  $\text{Co}^{2+}$  ( $S = \frac{3}{2}$ ) ions, and an diamagnetic octahedral  $\text{Co}^{3+}$  ( $S = 0$ ) ions.

means of an X'pert Pro (PANalytical) powder diffractometer with  $\text{Cu K}\alpha$  radiation in the Bragg–Brentano geometry. The data were recorded in the  $2\theta$  range of 15–128 deg. with the resolution of 0.01 deg. and the acquisition time of 6 s per step. Diffraction pattern was simulated by Rietveld method using the DBWS program,<sup>52</sup> according to the Young procedure.<sup>53</sup> The unit cell parameters were refined as cubic structure ( $Fd\bar{3}m$ , space group 227), and the starting parameters were taken from the ICSD file data 63164.

High resolution scanning transmission electron microscopy and parallel beam electron diffractions were carried out with a Hitachi dedicated STEM microscope operating at an accelerating voltage of 200 keV, and equipped with a field emission electron gun (FEG) together with Cs corrector of the spherical aberration. For the STEM experiments the powder specimens were deposited on a copper grid with the holey carbon thin film from alcohol solution and were cleaned with plasma generated from the mixture of hydrogen and oxygen gases for 20 s. Particle shapes were observed in the secondary electron image mode and the orientation was checked and reoriented by using the Kikuchi line diffraction pattern, obtained with the high convergence angle diffraction mode. Spot diffraction patterns were taken by parallel beam diffraction mode with beam diameter around 2 nm stopped on the particle. The fast Fourier transform was performed on high resolution images of atomic structure, taken in STEM brightfield imaging mode.

## RESULTS AND DISCUSSION

$\text{Co}_3\text{O}_4$  has a normal spinel structure ( $Fd\bar{3}m$ , space group 227), and the unit cell containing eight formula units (56 ions) exhibits a lattice constant  $a = 8.084 \text{ \AA}$ .<sup>54</sup> Cobalt cations occupy 8a and 16d Wyckoff positions at  $(\frac{1}{8}, \frac{1}{8}, \frac{1}{8})$  and  $(\frac{1}{2}, \frac{1}{2}, \frac{1}{2})$ , whereas oxygen atoms occupy the 32e oxygen positions at  $(u, u, u)$ , where  $u$  is the so-called oxygen parameter (Figure 1a). Only the lattice parameter  $a$  and the oxygen parameter  $u$  are required to completely determine the atomic positions of this structure. Distribution of the cations among the spinel interstitials can be characterized by the degree of inversion  $x$ . For  $\text{Co}_3\text{O}_4$  with  $x = 0$  half-field octahedral sites contain  $\text{Co}^{3+}(d^6)$  cations (denoted hereafter as  $\text{Co}^{\text{O}}$ ), whereas tetrahedral sites exhibiting one-eighth occupancy are filled by  $\text{Co}^{2+}(d^7)$  cations (denoted  $\text{Co}^{\text{T}}$ ).<sup>55</sup> Oxygen ions being

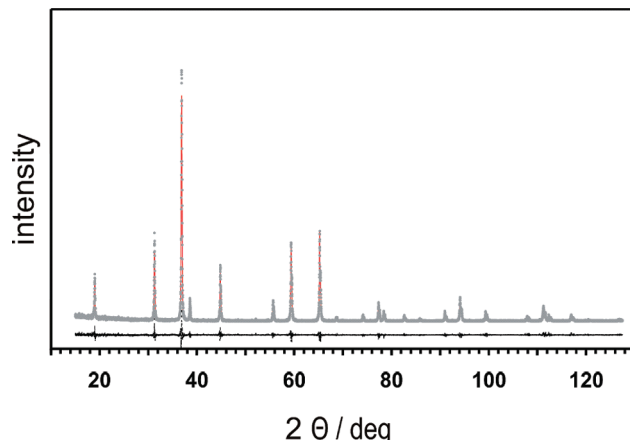


**Figure 2.** XRD pattern (gray points) together with Rietveld refinement (red line) of the nanostructured cobalt spinel.

surrounded by 1  $\text{Co}^{\text{T}}$  and 3  $\text{Co}^{\text{O}}$  cations exhibit a 4-fold coordination ( $\text{O}_{4c}$ ). This ideal site occupancy may be perturbed, however, by partial inversion ( $x > 0$ ). Weak magnetic interactions among the tetrahedral cobalt ions have been discussed recently,<sup>56</sup> and results in a low Néel temperature of 40 K.<sup>57,58</sup>

**Bulk Structure and Properties. Validation of the Computational Scheme.** Bulk properties of  $\text{Co}_3\text{O}_4$  were computed and compared with experimental data to verify the adequacy of the employed DFT approach. Experimental structural parameters were derived from the recorded XRD pattern of the  $\text{Co}_3\text{O}_4$  sample by means of the Rietveld refinement simulation (Figure 2), and the results are summarized in Table 2.

The optimized lattice constant ( $a_{\text{PW91}} = 8.051 \text{ \AA}$  and  $a_{\text{PW91+U}} = 8.060 \text{ \AA}$ ) are within  $\sim 0.4\%$  difference with the experimental value of  $8.082 \text{ \AA}$ . Previous plane-wave DFT calculations using other gradient functionals led to similar level of the accuracy.<sup>40</sup> The calculated octahedral cobalt–oxygen and tetrahedral cobalt–oxygen bond lengths were equal to  $d_{\text{Co}^{\text{O}}-\text{O}} = 1.917 \text{ \AA}$  and  $d_{\text{Co}^{\text{T}}-\text{O}} = 1.924 \text{ \AA}$ , respectively. Both values compare well with the experimental  $\text{Co}^{\text{O}}-\text{O}$  and  $\text{Co}^{\text{T}}-\text{O}$  bond distances (Table 2). The  $d_{\text{Co}^{\text{O}}-\text{O}}$  and  $d_{\text{Co}^{\text{T}}-\text{O}}$  bond lengths were derived from the value of  $u = 0.263$ , extracted from Rietveld refinement of the diffraction pattern (Figure 2), using the following

**Table 2. Calculated and Experimental Bulk Properties of  $\text{Co}_3\text{O}_4$** 

property	calculated value (DFT+U)	experimental value
unit cell parameter/ $\text{\AA}$	8.060	8.082 <sup>a</sup>
unit cell volume/ $\text{\AA}^3$	523.64	528.29 <sup>a</sup>
<i>u</i> parameter	0.263	0.263 <sup>a</sup>
$\text{Co}^T-\text{O}$ distance/ $\text{\AA}$	1.924	1.935 <sup>b</sup>
$\text{Co}^O-\text{O}$ distance/ $\text{\AA}$	1.917	1.920 <sup>b</sup>
octahedral angle ( $\text{O}-\text{Co}-\text{O}$ )/deg	96.3	90 <sup>b</sup>
	83.7	
tetrahedral angle ( $\text{O}-\text{Co}-\text{O}$ )/deg	109.47	-
electronic gap/eV	1.53	1.6

<sup>a</sup> Derived from Rietveld refinement simulations. <sup>b</sup> Calculated from experimental *u* value.

equations.<sup>59</sup>

$$\begin{aligned} d_{\text{Co}-\text{O}}^{\text{O}} &= a\sqrt{3u^2 + 2u - 3/8} \\ d_{\text{Co}-\text{O}}^{\text{T}} &= a\sqrt{3}(u - 1/4) \end{aligned} \quad (2)$$

Variation of the *u* parameter reflects the adjustment of the oxygen positions to accommodate differences in the actual radius of the  $\text{Co}^T$  and  $\text{Co}^O$  cations. When *u* increases with respect to the reference value of 0.250, characteristic of ideal spinel geometry, the tetrahedral bond length increases, whereas the octahedral bond length decreases. The bond length  $d_{\text{Co}^T-\text{O}} > d_{\text{Co}^O-\text{O}}$  is consistent with the crystal radius of the divalent high spin  $\text{Co}^T$  ( $r_{\text{Co}^T} = 0.72 \text{ \AA}$ ) greater than the crystal radius of the trivalent low spin  $\text{Co}^O$  ( $r_{\text{Co}^O} = 0.685 \text{ \AA}$  for low spin and  $r_{\text{Co}^O} = 0.75 \text{ \AA}$  for high spin configuration), implying different spin states of both cations, which is nicely confirmed by the more accurate calculations (vide infra).

The calculated spin magnetic moment of the divalent  $\text{Co}^T$  ions was found to be  $2.27 \mu_B$  and  $2.61 \mu_B$  for PW91 and PW91+U, respectively, and remains in good agreement with preceding calculations.<sup>46</sup> Each of the  $\text{Co}^T$  ions of high spin  $e^4t_2^3$  configuration is surrounded by four nearest neighbor  $\text{Co}^T$  ions of opposite spin, giving rise to an antiferromagnetic network (Figure 1b), in line with empirical observations.<sup>57,58</sup> The trivalent  $\text{Co}^O$  ions, as already mentioned, exhibit a closed shell  $t_{2g}^6$  configuration and consequently a nil magnetic moment, clearly revealed by spin density repartition within the unit cell (Figure 1b) and by the spin polarized band structure calculations (Figure 2). As a result the experimental magnetic state of cobalt spinel was well reproduced. The antiferromagnetic state was found to be situated about 0.1 eV below the energy level of a ferromagnetic alignment, again in line with magnetic studies.<sup>57,58</sup> The calculated value of the electronic gap of 1.53 eV compares well with the experimental value of 1.6 eV. The projected electronic density of states (DOS) for  $\text{Co}^O$ ,  $\text{Co}^T$ , and oxygen ions are discussed in more detail in Supporting Information S1.

We can thus reasonably assume that the employed formalism along with the used parametrization is capable to describe the  $\text{Co}_3\text{O}_4$  system with the adequate accuracy.

**Surface Energies and Reconstruction.** For surface energy modeling we considered three low index (100), (110), and (111) planes with the largest interplanar spacing, as they are predicted to be the most stable, following Bravais–Friedel–Donnay–Harker theory.<sup>60</sup> Indeed, a careful scrutiny of the experimental data reveals that only those planes are exposed in a number of  $\text{Co}_3\text{O}_4$  specimens prepared by various methods.<sup>9,61,62</sup>

**Table 3. Surface Energies Calculated with and without Inclusion of Hubbard *U* Parameter for  $\text{Co}_3\text{O}_4$  Spinel**

method	surface energy [ $\text{J}/\text{m}^2$ ]		
	(100)	(110)	(111)
DFT	1.38	1.65	1.48
DFT+U	1.38	1.65	1.47

Theoretical surface energies  $\gamma$  corresponding to the energy difference of the surface and bulk ions per unit area were calculated as follows:

$$\gamma = (E_{\text{slab}} - nE_{\text{bulk}})/2A \quad (3)$$

where  $E_{\text{slab}}$  denotes the slab energy and  $nE_{\text{bulk}}$  energy of the  $n \text{ Co}_3\text{O}_4$  units in the bulk model, whereas  $A$  is the surface exposed by the slab model for a given *hkl* plane. The entropic contribution can be added by using the computed full phonon density of states<sup>63</sup> or alternatively, in a simplified treatment, by inclusion of the most relevant vibration modes.<sup>64</sup> However, with quite good approximation we may neglect this term, which is a common approach in this type of calculations,<sup>25,10,21,65</sup> as it shall not affect the conclusions drawn in a significant way.<sup>23,28,25</sup> Indeed, crystal habits are principally determined by relative energies of the exposed planes, and entropy terms normally do not alter this ordering.<sup>25</sup> Groundwork DFT and DFT+U calculations for (100), (110), and (111) planes revealed that the surface energy is also quite insensitive to inclusion of the Hubbard parameter (Table 3). Therefore, all the calculations of the surface properties and shape prediction were performed within the DFT (GGA-PW91) approach alone.

For (100) plane modeling, we used a slab composed of 10 layers (8.35  $\text{\AA}$ ). Among possible terminations, the most stable structure of this plane consists of four coordinatively unsaturated 5-fold  $\text{Co}^O_{5c}$  (with one missing oxygen ligand), two recessed, fully coordinated 4-fold  $\text{Co}^T_{4c}$ , and two protruding 2-fold  $\text{Co}^T_{2c}$  ions (with two missing O ligands). The surface concentration of the  $\text{Co}^T$  ions ( $0.015 \text{ \AA}^{-2}$ ) is four times lower than the  $\text{Co}^O_{5c}$  ones ( $0.060 \text{ \AA}^{-2}$ ). The  $\text{Co}^O_{5c}$  cations located in truncated edge-sharing octahedra, constituted by five lattice  $\text{O}^{2-}$  anions, form regularly spaced strips joined sequentially by the  $\text{Co}^T$  cations (Figure 3a). The tetrahedral cobalt ions, in turn, are placed below the strips ( $\text{Co}^T_{4c}$  ions) and above them ( $\text{Co}^T_{2c}$  ions). The distance between the nearest  $\text{Co}^O$  cations is equal to 2.89  $\text{\AA}$ , whereas the tetrahedral cobalt species are separated by 8.051  $\text{\AA}$ . There are two types of exposed oxygen ions: the 4-fold  $\text{O}_{4c}$  species, preserving

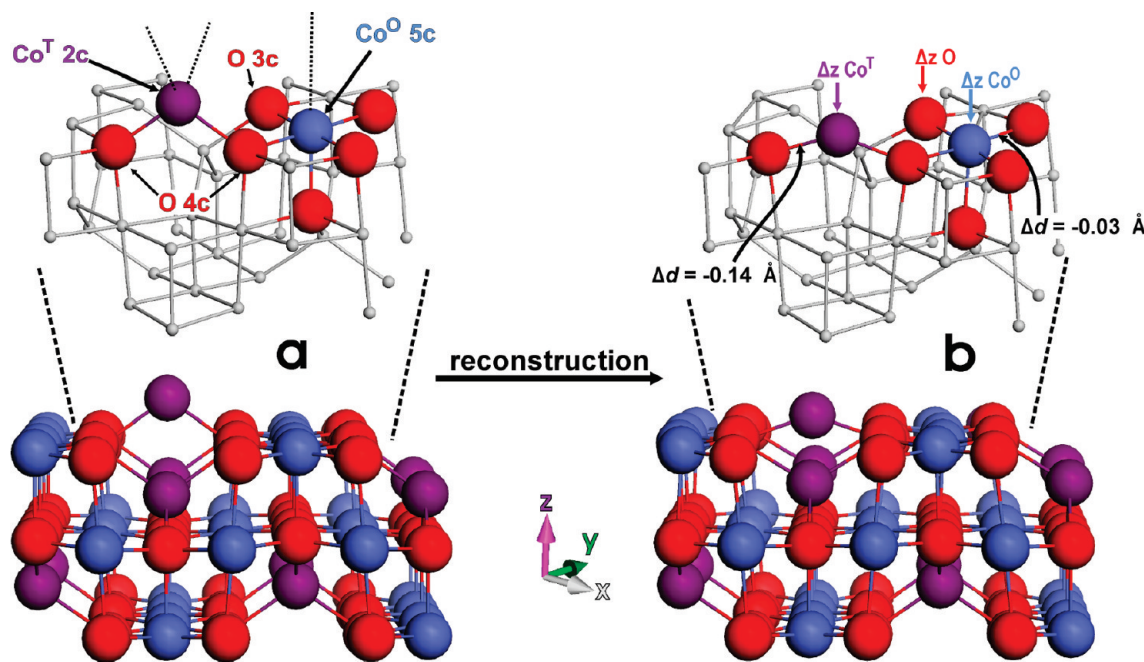


**Figure 3.** Top-lateral view of the optimized unrelaxed (a) and relaxed (b) structure of the (100) plane of  $\text{Co}_3\text{O}_4$ , with major displacements of the exposed ions marked by arrows.

bulk coordination, and truncated 3-fold  $\text{O}_{3c}$  ones (with one missing bond to  $\text{Co}^{\text{T}}$ ). In order to ensure equivalence of both surfaces in the slab model and preserve the surface stoichiometry, one  $\text{Co}^{\text{T}}$  cation per unit cell was displaced from upper to lower plane of the slab, giving rise to the following surface composition  $\{1\text{Co}^{\text{T}}_{2c}, 4\text{Co}^{\text{O}}_{5c}, 2\text{Co}^{\text{T}}_{4c}, 6\text{O}_{3c}, 2\text{O}_{4c}\}$  of the computational model for the (100) plane.

There are two principal types of terminations for the (110) surface, occasionally labeled as A and B in the literature.<sup>40</sup> They were modeled by slabs containing 7 (8.54 Å) and 9 layers (11.5 Å), respectively. The (110)-A plane is terminated with octahedral ions, the coordination of which is lowered to 4-fold ( $\text{Co}^{\text{O}}_{4c}$ ) one, which is caused by two missing oxygen bonds. The tetrahedral cobalt ions are surrounded by three oxygens, giving rise to 3-fold  $\text{Co}^{\text{O}}_{3c}$  surface centers (Figure 4a). The same trigonal coordination exhibit exposed oxygen anions ( $\text{O}_{3c}$ ). The (110)-B termination is a bit more deprived, exhibiting only 4-fold  $\text{Co}^{\text{T}}_{4c}$  cations and two types of 3-fold anions, with a  $\text{Co}^{\text{O}}(\text{O}_{3c})$  or a  $\text{Co}^{\text{T}}(\text{O}_{3c})$  neighbor missing. In contrast to the (100) plane, the concentration of both cobalt species, equal to  $0.044 \text{ \AA}^{-2}$  and  $0.033 \text{ \AA}^{-2}$  for  $\text{Co}^{\text{O}}$  and  $\text{Co}^{\text{T}}$ , respectively are comparable here. The  $\text{Co}^{\text{O}}-\text{Co}^{\text{O}}$  distance for the (110) plane was found to be 2.95 Å, whereas the  $\text{Co}^{\text{T}}-\text{Co}^{\text{T}}$  spacing equals to 3.48 Å (for A termination).

In order to ensure the proper stoichiometry and parity of the lower and upper planes the (110)-A termination was modified by removing one  $\text{Co}^{\text{T}}$  cation from both sides. The resultant computational model of the (110)-A plane exhibits the following composition  $\{3\text{Co}^{\text{T}}_{3c}, 4\text{Co}^{\text{O}}_{4c}, 4\text{O}_{3c}, 4\text{O}_{2c}\}$ . In the case of the (110)-B termination more sever modifications involving deletion of two cobalt and four oxygen atoms were needed. The resultant model of this termination consist of  $\{4\text{Co}^{\text{T}}_{3c}, 2\text{Co}^{\text{O}}_{3c}, 4\text{O}_{3c}, 4\text{O}'_{3c}\}$  surface ions. For further calculations only the more stable (110)-A plane, containing less dangling ions ( $\gamma_{(110)-\text{A}} = 1.65 \text{ J/m}^2$  and  $\gamma_{(110)-\text{B}} = 1.92 \text{ J/m}^2$ , *vide infra*), was taken into account.

The (111) plane was modeled using a slab comprising 13 layers (9.88 Å). Cleavage of  $\text{Co}_3\text{O}_4$  across this plane can produce six conceivable nonequivalent terminations. The most stable (111) surface with the smallest number of dangling bonds (Figure 5a) is characterized by strong under-saturation of four  $\text{Co}^{\text{O}}$  ions, which is reduced to 3-fold coordination ( $\text{Co}^{\text{O}}_{3c}$ ), whereas in the case of four  $\text{Co}^{\text{T}}$  only one  $\text{O}^{2-}$  ligand is lost ( $\text{Co}^{\text{T}}_{3c}$ ). The exposed oxygen ions, in turn, take account of ten  $\text{O}_{3c}$  and six  $\text{O}_{4c}$  species per unit cell. The concentration of both cobalt species is equal to  $0.018 \text{ \AA}^{-2}$  and  $0.036 \text{ \AA}^{-2}$  for  $\text{Co}^{\text{O}}$  and  $\text{Co}^{\text{T}}$ , respectively. The shortest  $\text{Co}-\text{Co}$  distance of 3.41 Å is larger than that observed for (100) and (110) planes, and is defined by the adjacent  $\text{Co}^{\text{O}}$  and  $\text{Co}^{\text{T}}$  ions (Figure 5a). In order to preserve the stoichiometry and equivalence of both surfaces of the slab, one  $\text{Co}^{\text{T}}$  ion was displaced from the upper into the lower plane, giving rise to the following composition  $\{4\text{Co}^{\text{T}}_{3c}, 2\text{Co}^{\text{O}}_{3c}, 10\text{O}_{3c}, 6\text{O}_{4c}\}$  of the computational model for the (111) plane.

Surface reconstruction for all investigated planes is significant only for the highly unsaturated surface ions, and can be described as prevailing relaxation in z-direction (toward the bulk). For the (100) termination the unsaturated  $\text{Co}^{\text{T}}_{2c}$  ions move about  $-0.45 \text{ \AA}$  inward and the  $\text{Co}^{\text{O}}-\text{O}_{3c}-\text{Co}^{\text{T}}$  central oxygen by  $-0.06 \text{ \AA}$ . The  $\text{Co}^{\text{O}}$  ions remained almost unperturbed (Table 4, Figure 3b). Those changes are accompanied by considerable reduction of the  $\text{Co}^{\text{O}}-\text{O}$  and  $\text{Co}^{\text{T}}-\text{O}$  bond lengths by  $-0.14 \text{ \AA}$  and  $-0.07 \text{ \AA}$ , respectively. A substantial increase of the  $\text{O}-\text{Co}^{\text{T}}_{2c}-\text{O}$  angles by 33.4 deg and almost intact  $\text{O}-\text{Co}^{\text{O}}_{5c}-\text{O}$  angles (with a mere drop of  $-4.2$  deg) were observed. For the (110) plane both the tetrahedral and the octahedral cobalt ions were considerably shifted inward by  $-0.25$  and  $-0.13 \text{ \AA}$ , respectively (Table 4, Figure 4b). Relaxation of the  $\text{Co}^{\text{O}}-\text{O}_{3c}-\text{Co}^{\text{T}}$  oxygen anion, up to  $-0.07 \text{ \AA}$  was close to that observed for the (100) plane. The shrinking of the  $\text{Co}^{\text{O}}-\text{O}$  bond ( $\Delta d_{\text{Co}^{\text{O}}-\text{O}} = -0.08 \text{ \AA}$  and  $-0.10 \text{ \AA}$ ) and the  $\text{Co}^{\text{T}}-\text{O}$  bond lengths ( $\Delta d_{\text{Co}^{\text{T}}-\text{O}} = -0.13 \text{ \AA}$  and  $-0.12 \text{ \AA}$ ) was more pronounced in this case. The associated changes in

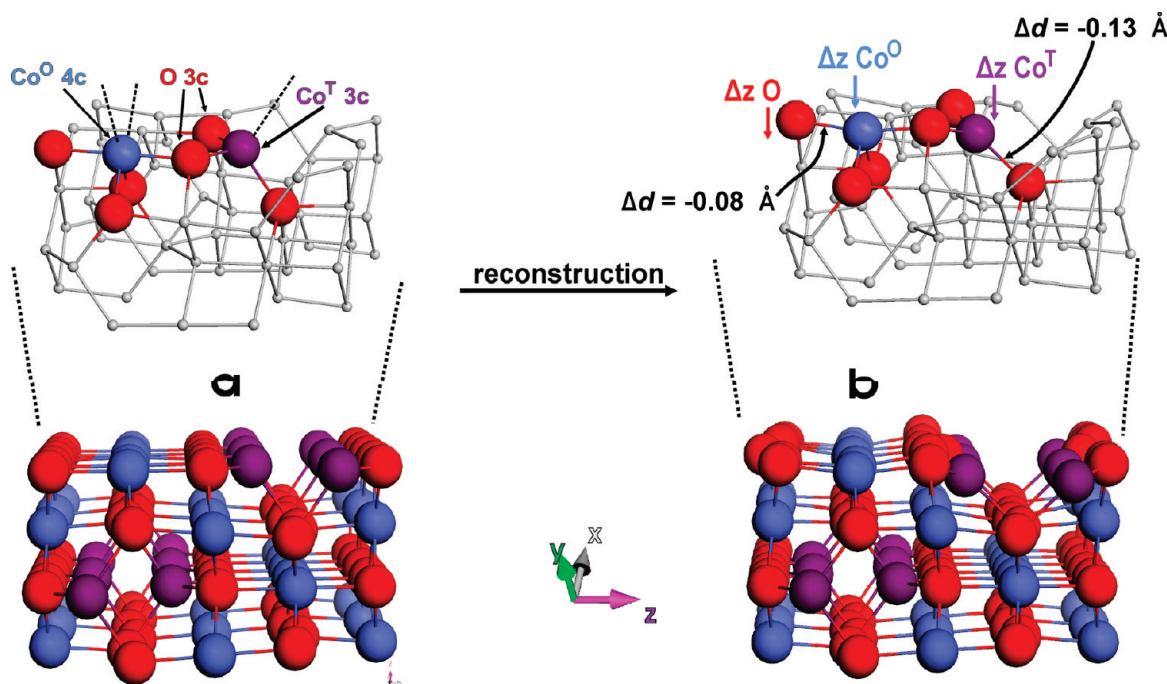


**Figure 4.** Top-lateral view of the optimized unrelaxed (a) and relaxed (b) structure of the (110) plane of  $\text{Co}_3\text{O}_4$ , with major displacements of the exposed ions marked by arrows.

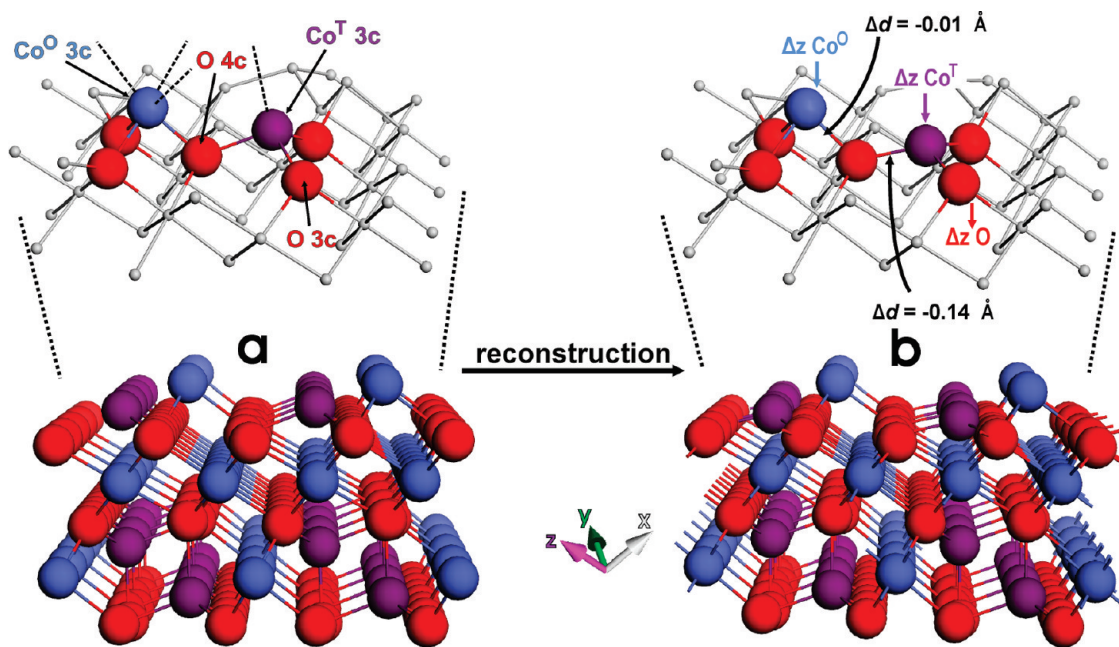


**Figure 5.** Top-lateral view of the optimized unrelaxed (a) and relaxed (b) structure of the (111) plane of  $\text{Co}_3\text{O}_4$ , with major displacements of the exposed ions marked by arrows.

the  $\text{O}-\text{Co}^{\text{T}}_{3\text{c}}-\text{O}$  angle by 11.1 deg. and the  $\text{O}-\text{Co}^{\text{O}}_{4\text{c}}-\text{O}$  angle by 4.2 deg. were both positive, in contrast to what was observed for the (100) plane.

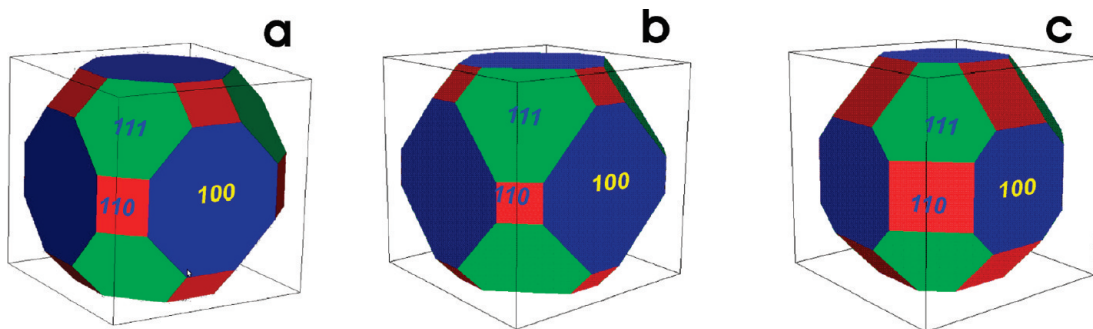
The highly unsaturated  $\text{Co}^{\text{O}}_{3\text{c}}$  ions in the (111) plane relax their position by moving along the  $z$ -axis by  $-0.06 \text{ \AA}$ , and similar displacement ( $-0.07 \text{ \AA}$ ) was observed for surface  $\text{O}_{3\text{c}}$  anions. Again, the most exposed tetrahedral  $\text{Co}^{\text{T}}$  ions shifted by  $-0.22 \text{ \AA}$ , exhibit the highest relaxation. The resultant contraction of the  $\text{Co}^{\text{O}}-\text{O}$

bond length was quite small ( $\Delta d_{\text{Co}^{\text{O}}-\text{O}} = -0.01 \text{ \AA}$ ) in contrast to more distinct decrease of the  $\text{Co}^{\text{T}}-\text{O}$  bond lengths ( $\Delta d_{\text{Co}^{\text{T}}-\text{O}} = -0.05 \text{ \AA}$  and  $-0.14 \text{ \AA}$ ). Furthermore, the reconstruction of the (111) surface involved rather small outward distortion of the  $\text{O}-\text{Co}^{\text{T}}_{3\text{c}}-\text{O}$  and the  $\text{O}-\text{Co}^{\text{O}}_{3\text{c}}-\text{O}$  angles (Table 4, Figure 5b).

The relaxation described above is responsible for considerable lowering of the surface energy by 0.19, 0.21, and  $0.28 \text{ J/m}^2$  for the (100), (110) and (111) planes, respectively, in comparison to the

**Table 4.** Surface Energy and Relaxation for the Most Stable (100), (110), and (111) Planes of  $\text{Co}_3\text{O}_4$ 

plane	$\gamma/\text{J}\cdot\text{m}^{-2}$		$\Delta z/\text{\AA}$			$\Delta d/\text{\AA}$		$\Delta\alpha/\text{deg}$	
	rigid	relaxed	$\text{Co}^T$	$\text{Co}^O$	O	$\text{Co}^O-\text{O}$	$\text{Co}^T-\text{O}$	$\text{O}-\text{Co}^T-\text{O}$	$\text{O}-\text{Co}^O-\text{O}$
(100)	1.57	1.38	-0.45	-0.01	-0.06	-0.03	-0.14 -0.07	33.4	-4.2
(110)	1.86	1.65	-0.25	-0.13	-0.07	-0.08 -0.10	-0.13 -0.12	11.1	3.1
(111)	1.75	1.48	-0.22	-0.06	-0.07	-0.01	-0.05 -0.14	7.2	4.4

**Figure 6.** Theoretical shapes for nanocrystalline  $\text{Co}_3\text{O}_4$  (a) calculated without surface reconstruction, (b) including surface reconstruction and (c) experimental shape retrieved by means of the Wulff method.

parent geometries. The calculated  $\gamma$  values for the rigid and relaxed surfaces together with the most important displacements of the surface ions along with the changes in the nearest cobalt–oxygen distances and angles observed upon the relaxation are collected in Table 4.

Although calculations of the surface energies for the (110) and (111) planes of cobalt spinel have been already undertaken by other authors,<sup>40</sup> a consistent and complete set of  $\gamma$  values is required to provide an appropriate input for reliable theoretical shape modeling, and this is performed for the first time in this paper. We have also found that the (110)-A termination is more stable than the (110)-B one, in contrast to previous data obtained with PBE functional.<sup>40</sup>

For validation of the results, we have used the computed surface energies from Table 4 to visualize the equilibrium morphologies of the relaxed and unrelaxed spinel crystals, using the Wulff construction (Figure 6, parts a and b). The resultant theoretical rhombicuboctahedral crystals expose predominantly six (100) and eight (111) low energy facets, truncated by 12 minor (110) planes of higher energy. The computed shape can be next compared with the morphology of the synthesized  $\text{Co}_3\text{O}_4$  nanocrystals, retrieved by matching the corresponding STEM images to the predicted three-dimensional rhombicuboctahedral shape, by means of the Wulffman software (Figure 6c). As implied by Figure 6, relaxation of the surface geometry leads to preferential development of the (111) planes at the expense of the (110) ones.

Selected projections of the reconstructed polyhedral shapes of the  $\text{Co}_3\text{O}_4$  crystallites, the high resolution Cs-corrected STEM images at two magnifications of the synthesized nanoparticles together with the corresponding Fast Fourier Transform (FFT) patterns are gathered in Figure 7. The high resolution images and parallel beam electron diffractions (see inserts in Figure 7a1–c1) revealed that the observed spinel nanoparticles were single crystals.

Furthermore, the nanoparticles are faceted on the (100), (111), and (110) planes, in excellent agreement with the theoretical calculations (Figure 7a–c). The indicated spacing of 0.292 and 0.491 nm corresponds well to the interlayer distances of the (110) and (111) crystallographic planes of  $\text{Co}_3\text{O}_4$ , respectively (Figure 7a2–c2). The symmetry of the diffraction spots in the FFT patterns (Figure 7a3–c3) reveals the orientation of the observed faceted particles along the [100], [110] and [111] axes, allowing for univocal alignment of the predicted 3D Wulff shapes with respect to the experimental 2D images.

The angles measured between the exposed facets, 125 deg, 135 deg, and 145 deg (Figure 7, parts a1, b1, and c1), are consistent with those expected between the (100)/(111), (100)/(110) and (110)/(111) planes of the spinel  $F\bar{d}3m$  structure. This confirms that, indeed, the observed polyhedrons assume the computed rhombicuboctahedral habit.

The presented nanocrystallites observed by STEM (Figure 7) were selected from larger population, the fragment of which is shown in Supporting Information (Figure S2). As can be seen therein, in the synthesized material we observed exclusively the spinel nanocrystals with the exposed (111), (110), and (100) facets. Depending on their abundance the crystallites assumed the predominant rhombicuboctahedral shape with the prevailing (100) and (111) planes or less frequent truncated octahedral shapes with the main (110) plane. The actual morphology is a matter of thermodynamic and kinetic factors as discussed below. However, for comparison with the Wulff derived theoretical habits only those exhibiting equilibrium shapes can meaningfully be taken into account.

Closer inspection of Figure 6 and Figure 7 revealed some appreciable differences between the morphologies of the pristine Wulff construction and the experimental habit (manifested mainly by a slightly enlarged abundance of the (110) plane). The stability of nanoparticles is gauged by the Gibbs energy

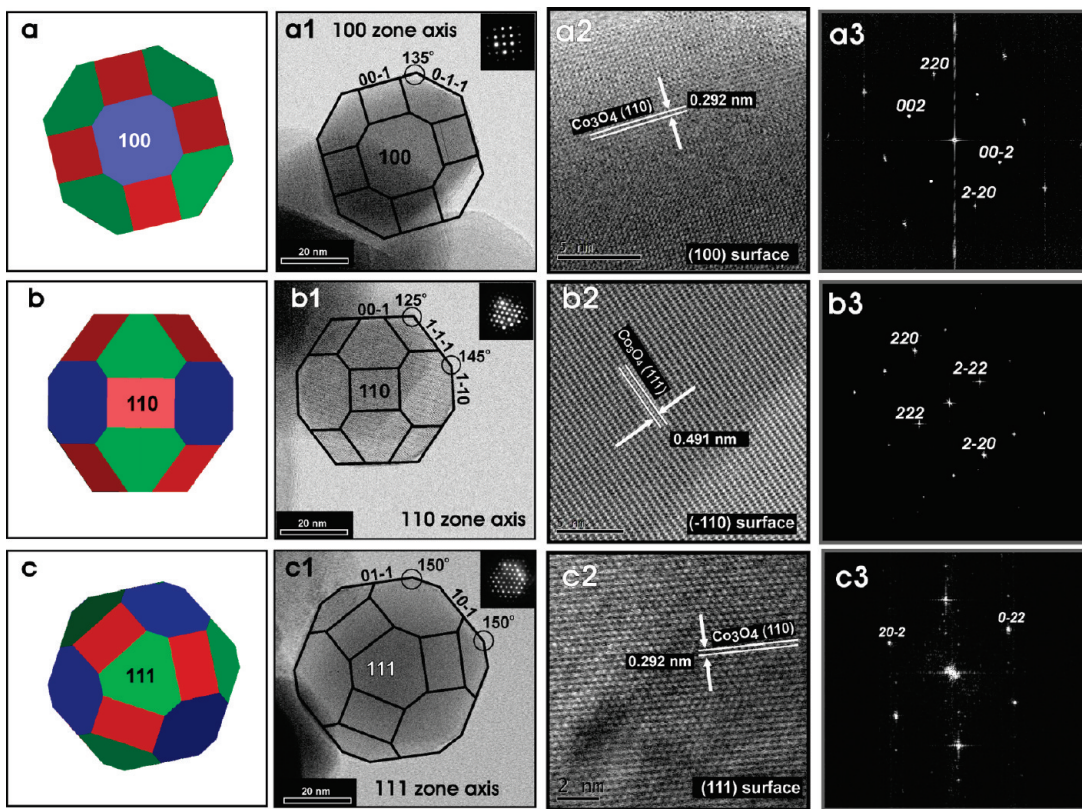


**Figure 7.** Thermodynamical Wulff shape (a–c) together with reconstructed STEM shapes (a1–c1) of cobalt nanocrystals viewed along the [100], [110], and [111] directions. HRTEM images of the exposed  $\text{Co}_3\text{O}_4$  planes (a2–c2), together with the corresponding fast Fourier transform (a3–c3) indexed within the  $Fm\bar{3}m$  space group.

$G(T) = G_{\text{bulk}}(T) + G_{\text{surf}}(T) \approx \Delta_f G^\circ + (M/\rho)q\sum_i f_i \gamma_i$ , where  $M$  is the molar mass,  $\rho$  is the density,  $q$  is the surface-to-volume ratio, and  $f_i$  are weight factors for surface energies  $\gamma_i$ .<sup>21</sup> Substitution of the computed numerical values showed that the total surface energy normalized to the volume of the nanocrystal of an average size,  $V_{\text{ncryst}} = 55809 \text{ nm}^3$ , changes from 1.095 to 1.111  $\text{fJ}$  for the DFT-predicted and the experimental shapes, respectively. Such small enhancement of the surface energy by 1.5% can certainly be accommodated by the limited accuracy of the adopted model. In the most straightforward way, this phenomenon can be accounted for by residual hydroxylation of the surface (not taken into account), which obviously modifies the energy of the exposed planes.<sup>66</sup> However, our calculation of surface energy of the hydroxylated planes revealed that in such a case the abundance of the exposed (110) planes is disfavored by adsorbed water (Supporting Information, Figure S3). Furthermore, comparison of the calculated habit of the  $\text{Co}_3\text{O}_4$  nanocrystals in dry ( $\Theta_{\text{OH}/\text{H}_2\text{O}} = 0$ ) and wet conditions ( $\Theta_{\text{OH}/\text{H}_2\text{O}} = 0.8$ ) indicates that hydroxylation has only a slight effect on the overall spinel morphology<sup>66</sup> and cannot be associated with the observed minor contribution of the truncated octahedral shapes.

It is well-known, that appearance of the crystallites may also be influenced by anisotropy in the rate of crystal growth, under particular experimental conditions (Wulff–Chernov plot).<sup>17,22,27</sup> In the case of nanocrystals that have still not reached the equilibrium, but are in the stage of a steady-state growth, the lowest perpendicular extension rate  $v_{\text{hkl}}(n)$  modifies the shape, asymptotically evolving into the thermodynamic habit. By proper adjusting the relative speed of growth for different terminations ( $v_{100}: v_{110}: v_{111} =$

1:0.88:0.95) both shapes can be match satisfactorily. The total surface energy of the resultant average-size nanocrystal (with the same volume of  $55809 \text{ nm}^3$ ) was assessed to be equal to 1.045  $\text{fJ}$ , using the experimental  $\gamma$ -values. It is only slightly smaller than that obtained in the DFT calculations, suggesting that in fact there is no substantial difference between thermodynamic stability of the predicted and observed shapes. Therefore, a plausible origin of the observed fine differences in the morphology can be associated with the kinetic effects quite reasonably. Indeed, the observed minor truncated octahedral nanocrystals can be associated with only slightly slower speed of growth of the (111) plane ( $v_{100}:v_{110}:v_{111} = 1:1:0.88$ ). Current more comprehensive work carried out in our laboratory includes size effects or the extent of surface complexation, in accounting for the experimental morphologies of the  $\text{Co}_3\text{O}_4$  nanostructures obtained in various conditions.

Once the polyhedral form of the crystallites is determined, from the areas of the exposed planes, we can calculate their fractional abundance, total surface area, and the areal concentration of cobalt ions. Such data are useful for calculation of turnover frequencies or for establishing quantitative relationships between preparation conditions and profusion of specific crystallographic facets that are catalytically most active, allowing for development of improved catalytic materials based on cobalt spinel structure.<sup>37,36</sup> Such studies belong to one of the leading direction in shape dependent nanocatalysis on oxides including cobalt spinel, where controlled faceting allows for optimization of its catalytic properties. In fact, the (100) plane has been found to be the most active in  $\text{N}_2\text{O}$  decomposition reaction,<sup>36</sup> the (110) has

been recognized much more active than (100) for CH<sub>4</sub> activation and CO oxidation,<sup>11,67</sup> whereas the (111) plane populated by highly unsaturated ions, being easily contaminated by inhibitors, such as water,<sup>68</sup> seems to be catalytically less important.

## CONCLUSIONS

The bulk structure, shape, and surface energies of the low index (100), (110), and (111) planes exposed by Co<sub>3</sub>O<sub>4</sub> nanocrystals were investigated by means of periodic PW91 and PW91+U density functional (DFT) calculations, combined with high resolution STEM studies. The calculated surface energies  $\gamma$  for the relaxed planes were found to increase in the following order 1.38 J m<sup>-2</sup> (100) < 1.48 J m<sup>-2</sup> (111) < 1.65 J m<sup>-2</sup> (110). The consistent set of computed  $\gamma$  values was used to predict the equilibrium shape of Co<sub>3</sub>O<sub>4</sub> crystallites using Wulff construction. The rhombicuboctahedral habit predicted by DFT modeling compares well with the experimental shape of the synthesized spinel nanocrystals, retrieved by matching the corresponding 2D TEM images to 3D Wulff shapes for three principal [100], [110], and [111] directions.

## ASSOCIATED CONTENT

**S Supporting Information.** Detailed information on the cobalt spinel electronic structure, STEM picture of Co<sub>3</sub>O<sub>4</sub> nanocrystallites and Wulff shapes of dry and partially hydroxylated Co<sub>3</sub>O<sub>4</sub>. This material is available free of charge via the Internet at <http://pubs.acs.org>.

## AUTHOR INFORMATION

### Corresponding Author

\*E-mail: sojka@chemia.uj.edu.pl. Telephone: +48 12 663 22 95. Fax: +48 12 634 05 15.

## ACKNOWLEDGMENT

This work was carried out within the COST action D41 Inorganic Oxides, and supported by 299/N- COST/208/0 project of MNiSzW. The research was partially carried out with the equipment purchased thanks to financial support from the European Regional Development Fund in the framework of the Polish Innovation Economy Operational Program (Contract No. POIG.02.01.00-12-023/08).

## REFERENCES

- (1) Al-Abadleh, H. A.; Grassian, V. H. *Surf. Sci. Rep.* **2003**, *52*, 63.
- (2) Puntas, V. F.; Krishnan, K. M.; Alivisatos, A. P. *Science* **2001**, *291*, 2115.
- (3) McKenna, K. P.; Sushko, P. V.; Shluger, A. L. *J. Am. Chem. Soc.* **2007**, *129*, 8600.
- (4) Ganduglia-Pirovano, M. V.; Hofmann, A.; Sauer, J. *Surf. Sci. Rep.* **2007**, *62*, 219.
- (5) Di Valentin, C.; Finazzi, E.; Pacchioni, G.; Selloni, A.; Livraghi, S.; Czoska, A. M.; Paganini, M. C.; Giannello, E. *Chem. Mater.* **2008**, *20*, 3706.
- (6) Sojka, Z.; Giannello, E.; Che, M.; Zecchina, A.; Dyrek, K. *J. Phys. Chem.* **1988**, *92*, 1541.
- (7) Di Valentin, C.; Pacchioni, G.; Selloni, A. *Chem. Mater.* **2005**, *17*, 6656.
- (8) Bromley, S. T.; Moreira, I. D. P. R.; Neyman, K. M.; Illas, F. *Chem. Soc. Rev.* **2009**, *38*, 2657.
- (9) Somorjai, G. A.; Park, J. Y. *Angew. Chem., Int. Ed.* **2008**, *47*, 9212.
- (10) Chizallet, C.; Costentin, G.; Lauron-Pernot, H.; Krafft, J.-M.; Che, M.; Delbecq, F.; Sautet, P. *J. Phys. Chem. C* **2008**, *112*, 16629.
- (11) Xie, X.; Shen, W. *Nanoscale* **2009**, *1*, 50.
- (12) Cushing, B. L.; Kolesnichenko, V. L.; O'Connor, C. *J. Chem. Rev.* **2004**, *104*, 3893.
- (13) Mao, Y.; Park, T. J.; Zhang, F.; Zhou, H.; Wong, S. S. *Small* **2007**, *3*, 1122.
- (14) Wulff, G. Z. *Kristallogr.* **1901**, *34*, 449.
- (15) Herring, C. *Phys. Rev.* **1951**, *82*, 87.
- (16) Roosen, A. R.; McCormack, R. P.; Carter, W. C. *Comput. Mater. Sci.* **1998**, *11*, 16.
- (17) Chernov, A. A. *Sov. Phys. Crystallogr.* **1963**, *7*, 728.
- (18) Feldhoff, A.; Mendive, C.; Bredow, T.; Bahnemann, D. *Chem. Phys. Chem.* **2007**, *8*, 805.
- (19) Friedrich, H.; de Jongh, P. E.; Verkleij, A. J.; de Jong, K. P. *Chem. Rev.* **2009**, *109*, 1613.
- (20) Xu, X.; Saghi, Z.; Gay, R.; Möbus, G. *Nanotechnology* **2007**, *18*, 225501.
- (21) Barnard, A. S.; Zapol, P. *J. Chem. Phys.* **2004**, *121*, 4276.
- (22) Barnard, A. S.; Zapol, P. *J. Phys. Chem. B* **2004**, *108*, 18435.
- (23) Vittadini, A.; Casarin, M.; Selloni, A. *J. Phys. Chem. C* **2009**, *113*, 18973.
- (24) Raybaut, P.; Dinge, M.; Iftimie, R.; Wellens, W.; Euzen, P.; Toulhoat, H. *J. Catal.* **2001**, *201*, 236.
- (25) Baetzold, R.; Yang, H. *J. Phys. Chem. B* **2003**, *107*, 14357.
- (26) Zhao, N.; Ma, W.; Cui, Z.; Song, W.; Xu, C.; Gao, M. *ACS Nano* **2009**, *3*, 1775.
- (27) Geysermans, P.; Finocchi, F.; Goniakowski, J.; Hacquart, R.; Jupille, J. *Phys. Chem. Chem. Phys.* **2009**, *11*, 2228.
- (28) Rogal, J.; Reuter, K.; Scheffler, M. *Phys. Rev. B* **2004**, *69*, 075421.
- (29) Stroppa, D.; G. Montoro, L. A.; Beltran, A.; Conti, T. G.; da Silva, R. O.; Andres, J.; Longo, E.; Leite, E. R.; Ramirez, A. *J. Am. Chem. Soc.* **2009**, *131*, 14544.
- (30) Wang, Y.; Xia, H.; Lu, L.; Lin, J. *ACS Nano* **2010**, *4*, 1425.
- (31) Grimes, N. W. *Phys. Techn.* **1975**, *6*, 22.
- (32) Zecchina, A.; Scarano, D.; Bordiga, S.; Spoto, G.; Lamberti, C. *Adv. Catal.* **2001**, *46*, 265.
- (33) Jansson, J.; Skoglundh, M.; Fridell, E.; Thormählen, P. *Top. Catal.* **2001**, *38*, 16.
- (34) Broqvist, P.; Panas, I.; Persson, H. *J. Catal.* **2002**, *210*, 198.
- (35) Yan, L.; Ren, T.; Wang, X.; Gao, Q.; Ji, D.; Suo, J. *Catal. Commun.* **2003**, *4*, 505.
- (36) Zasada, F.; Stelmachowski, P.; Maniak, G.; Paul, J. F.; Kotarba, A.; Sojka, Z. *Catal. Lett.* **2009**, *127*, 126.
- (37) Stelmachowski, P.; Zasada, F.; Maniak, G.; Granger, P.; Inger, M.; Wilk, M.; Kotarba, A.; Sojka, Z. *Catal. Lett.* **2009**, *130*, 637.
- (38) Yakovlev, A. L.; Zhidomirov, G. M.; Van Santen, R. *Catal. Lett.* **2001**, *75*, 418.
- (39) Mai, H. X.; Sun, L. D.; Zhang, Y. W.; Si, R.; Feng, W.; Zhang, H. P.; Liu, H. C.; Yan, C. H. *J. Phys. Chem. B* **2005**, *109*, 24380.
- (40) Xu, X. L.; Chen, Z. H.; Li, Y.; Chen, W. K.; Li, J. Q. *Surf. Sci.* **2009**, *603*, 653.
- (41) Hafner, J. *J. Comput. Chem.* **2008**, *29*, 2046.
- (42) Mermin, N. D. *Phys. Rev.* **1965**, *137*, A1141.
- (43) Bloch, P. E. *Phys. Rev. B* **1994**, *50*, 17953.
- (44) Kresse, G.; Joubert, D. *Phys. Rev. B* **1999**, *59*, 1758.
- (45) Perdew, J. P.; Wang, Y. *Phys. Rev. B* **1992**, *45*, 13244.
- (46) Walsh, A.; Wei, S. H.; Yan, Y.; Al-Jassim, M. M.; Turner, J. A. *Phys. Rev. B* **2007**, *76*, 165119.
- (47) Monkhorst, H. J.; Pack, J. D. *Phys. Rev. B* **1976**, *13*, 5188.
- (48) Methfessel, M.; Paxton, A. T. *Phys. Rev. B* **1989**, *40*, 3616.
- (49) Knop, O.; Reid, K. I. E.; Sutaru, O.; Nakagawa, Y. *Can. J. Chem.* **1968**, *46*, 3463.
- (50) <http://www.ctcms.nist.gov/wulffman/>
- (51) <http://www.geomview.org/>
- (52) Young, R. A.; Sakthivel, A.; Moss, T. S.; Paiva-Santos, C. O. J. *Appl. Crystallogr.* **1995**, *28*, 366.

- (53) Young, R. A., Ed. *The Rietveld Method*; Oxford University Press: Oxford, U.K., 1993.
- (54) Liu, X.; Prewitt, C. T. *Phys. Chem. Miner.* **1990**, *17*, 168.
- (55) Smith, W. L.; Hobson, A. D. *Acta Crystallogr. B* **1973**, *29*, 362.
- (56) Lee, S. G.; Balents, L. *Phys. Rev B* **2008**, *78*, 144417.
- (57) Roth, W. L. *J. Phys. Chem. Solids* **1964**, *25*, 1.
- (58) Dutta, P.; Seehra, M. S.; Thota, S.; Kumar, J. *J. Phys.: Condens. Matter* **2008**, *20*, 015218.
- (59) Hill, R. J.; Craig, J. R.; Gibbs, G. V. *Phys. Chem. Miner* **1979**, *4*, 317.
- (60) Docherty, R.; Clydesdale, G.; Roberts, K. J.; Bennema, P. *J. Phys. D: Appl. Phys.* **1991**, *24*, 89.
- (61) Xu, R.; Chun-Zeng, H. *J. Phys. Chem. B* **2003**, *107*, 926.
- (62) Liu, X.; Qiu, G.; Li, X. *Nanotechnology* **2005**, *16*, 3035.
- (63) Heid, R.; Pintschovius, L.; Reichardt, W.; Bohnen, K. P. *Phys. Rev. B* **2000**, *61*, 12059.
- (64) McBride, J. R.; Hass, K. C.; Weber, W. H. *Phys. Rev. B* **1991**, *44*, 5016.
- (65) Hamad, S.; Cristol, S.; Catlow, C. R. A. *J. Phys. Chem. B* **2002**, *106*, 11002.
- (66) Zasada, F.; Piskorz, W.; Cristol, C.; Paul, J.-F.; Kotarba, A.; Sojka, Z. *J. Phys. Chem. C* **2010**, *114*, 22245.
- (67) Hu, L.; Peng, Q.; Li, Y. *J. Am. Chem. Soc.* **2008**, *130*, 16136.
- (68) Petitto, S. C.; Marsh, E. M.; Garson, G. A.; Lengell, M. A. *J. Mol. Catal. A: Chem.* **2008**, *281*, 49.